The Laser Treatment's Impact on the Surface Topography of MONEL® Alloy 400, used in the Manufacturing of Marine Equipment Components

Assoc. Prof. Ph.D. Eng. **Ștefan ŢĂLU**[1,*], M.Sc. **Kipkurui RONOH**[2,3,4], Assoc. Prof. Ph.D. **Dinara SOBOLA**[2,3,5]

[1] Technical University of Cluj-Napoca, The Directorate of Research, Development and Innovation Management (DMCDI), Constantin Daicoviciu Street, no. 15, Cluj-Napoca, 400020, Cluj county, Romania.

[2] Brno University of Technology, Central European Institute of Technology, Purkyňova 123, 612 00 Brno, Czech Republic. e-mails: kipkurui.ronoh@ceitec.vutbr.cz, sobola@vut.cz

[3] Brno University of Technology, Faculty of Electrical Engineering and Communication, Department of Physics, Technická 2848/8, 616 00 Brno, Czech Republic.

[4] Dedan Kimathi University of Technology, Department of Mechanical Engineering, Private Bag 10143, Dedan Kimathi, Nyeri, Kenya.

[5] Czech Academy of Sciences, Institute of Physics of Materials, Žižkova 22, 61662 Brno, Czech Republic.

* stefan_ta@yahoo.com

Abstract: *In the study, the authors investigated the effects of picosecond laser ablation on the surface topographies of MONEL® alloy 400, used in the manufacturing of marine equipment components (such as pumps, valves, fixtures and fasteners). The experimental methodology involved preparing the material through grinding, polishing, and cleaning before subjecting it to picosecond laser ablation using specific parameters. The laser processing was carried out to create square ablated cavities on the alloy surface. The impact of the laser treatment on the surface condition of the alloy was assessed through profilometry analysis. The results provide insights into the surface topographies of the laser-treated MONEL® alloy 400 samples, offering valuable information for potential applications in marine industries.*

Keywords: *Laser treatment, marine equipment components, MONEL® alloy 400, surface topography*

1. Introduction

Monel® alloy 400, a nickel-copper alloy with a single-phase, and face-centered cubic structure, comprises at least 63% nickel and 28-34% copper with trace amounts of iron, manganese, silicon, sulfur. Monel® alloy 400 has exceptional resistance to corrosive agents such as seawater, high-temperature steam, salt, and caustic solutions [1-3]. It derives its robustness from its solid solution nature, rendering it susceptible to hardening solely through cold working processes [1, 4]. This alloy's composition grants it a suite of desirable properties, including corrosion resistance, weldability, and high tensile strength. In environments characterized by the rapid flow of seawater, Monel® alloy 400 demonstrates a low corrosion rate, coupled with impressive resistance to stress-corrosion cracking in most freshwater settings. These attributes, combined with its ability to withstand a variety of corrosive conditions, have propelled its widespread adoption in marine applications and other environments featuring non-oxidizing chloride solutions.
Monel® alloy 400 exhibits exceptional resistance to hydrochloric and hydrofluoric acids in de-aerated conditions, due to its resilience in challenging chemical environments. However, its high copper content renders it susceptible to rapid corrosion when exposed to nitric acid and ammonia systems [5-7]. Even in subzero temperatures, Monel® alloy 400 maintains remarkable mechanical properties, making it suitable for a diverse range of applications [6, 8]. It can withstand temperatures up to 538°C, with a melting point ranging between 1292-1349°C. Nonetheless, its strength in the annealed state is relatively low, necessitating the use of various tempers to enhance its mechanical robustness. Also, it is commonly employed in the manufacturing of valves, pumps, shafts, fittings, and fasteners for its exceptional corrosion resistance and mechanical strength. In industrial settings, Monel® alloy 400 is used in heat exchangers and plays a major role in processes involving chlorinated solvents and crude oil distillation towers [6, 9].

Lasers are indispensable tools in material processing, drawing significant attention in both scientific research and advanced manufacturing applications [4-6, 8, 9]. Ultrafast lasers, notably the picosecond (ps) laser, excel due to their high peak power and rapid pulse duration (10^{-12} s) within the material, resulting in high precision in material removal. The short pulse duration ensures that energy is deposited into the material quickly, leading to rapid vaporization and ablation of the targeted area without imparting excessive heat to the surrounding regions. This phenomenon not only enhances the overall machining efficiency but also contributes to the preservation of material properties and dimensional accuracy. Additionally, ultrafast lasers excel in minimizing heat-affected zones (HAZ), preventing the formation of cracks and recasts, and ensuring high integrity and quality of the machined surface [4].

While numerous studies have explored ultrafast laser processing of materials across various environmental conditions, research regarding its application specifically for Monel® alloy 400 remains limited [4, 8, 9]. There is still a lack of comprehensive understanding regarding how laser parameters impact the formation of various nano/microstructures on Monel® alloy 400.

In engineering product design and manufacturing, it is widely acknowledged that the 3-D surface topography significantly influences product functionality and quality [10-13]. Engineering surfaces typically exhibit characteristics such as randomness, isotropy or anisotropy, and can be categorized as Gaussian or non-Gaussian [14].

Various techniques are used to quantify surface morphology, encompassing the physical structure and features present on a surface, enabling researchers to analyze its shape, roughness, microtexture, and other geometric properties [15-21].

Statistical analysis of a surface morphology, following ISO 25178-2:2012 [22], entails applying statistical methods to quantify parameters like roughness and texture, providing insights into surface characteristics and behavior. By statistically analyzing the surface data, researchers can gain insights into the distribution and variability of surface features, allowing for a comprehensive understanding of the nanostructure's characteristics and behavior [23, 24].

Another approach, fractal and multifractal geometry offers innovative models to characterize surface roughness, assessing the full range of surface variations, and providing insight into their spatial complexity across all scales using scale-independent parameters [25-31].

A novel method, the Minkowski Functionals (MFs) provides a mathematical framework for characterizing the morphological attributes of surface topography, offering quantitative measures of geometric properties such as area, perimeter, curvature, and connectivity. This enables a comprehensive assessment of surface morphology, aiding in the interpretation of surface properties and their impact on material behavior and performance [32-36].

This research aimed to investigate how laser processing and scanning parameters influence the surface morphology and topography evolution of processed surfaces of marine equipment components on Monel® alloy 400.

2. Experimental methodology

In this study Monel® alloy 400 (UNS N04400), a commercially available alloy, was considered for investigation. Prior to laser processing, the material underwent a preparatory sequence, beginning with mechanical fine grinding followed by polishing to achieve a mirror-like surface finish. Subsequently, the sample underwent ultrasonic cleaning using acetone and ethanol for 10 minutes each, followed by drying with pressurized air to eliminate any surface impurities. The laser processing of the alloy was carried out utilizing a picosecond (ps) laser system (Perla® 100, Hilase, Dolní Břežan, Czech Republic) [37]. This laser system is distinguished by its capability to generate extremely short pulses in the picosecond range, operating at a wavelength of 1030 nm. Each pulse has a duration of 1 ps, with a maximum energy output of 1 mJ per pulse, and operates at a repetition rate of 60 kHz. A focusing lens (Linos, Qioptiq, Göttingen, Germany) with a focal length of 100 mm was employed to precisely focus the laser beam onto the surface at a perpendicular angle, resulting in a focused diameter of approximately 25 μm. The scanning head (intelliSCAN 14, Scanlab GmbH, Puchheim, Germany) facilitated the controlled movement of the linearly polarized laser beam across the surface, enabling precise laser processing of the samples [38].

Laser ablation experiments were conducted using various laser fluences and other parameters, as detailed in Table 1.

Table 1: Laser processing parameters used

Parameters	**Values [-]**			
Sample	A	B	C	D
Laser fluence [J/cm^2]	1	4	8	15
Scanning velocity [mm/s]	100	100	100	100
Hatching distance [μm]	5	5	5	5
Scanning pass [-]	1	1	1	1

The sample was securely positioned on an X-Y table, oriented perpendicular to the incident laser beam, with each sample subjected to processing within ambient air, covering a surface area of 2.0 x 2.0 mm². Patterning design generation was facilitated using the Direct Machining Control 1.7.60 (64 bit) software (Direct Machining Control, Vilnius, Lithuania). Laser raster scanning was executed in orthogonal directions: horizontally (0°) in the initial layer and vertically (90°) in the subsequent layer, employing bidirectional scan trajectories to generate square ablated cavities. Following laser ablation, the samples underwent cleaning in ethanol within an ultrasonic bath for 10 minutes to remove contaminants and solid debris from the laser-ablated surfaces. To evaluate the impact of picosecond laser treatment on the surface condition of Monel® alloy 400, the laser-ablated samples were subjected to characterization post-surface irradiation.
A series of five test surfaces of samples were analyzed and compared based on their 3-D surface texture characteristics using a profilometer (Dektak XT, Bruker, Billerica, MA, USA), having a profilometer tip with a radius of 2 μm for measurements. Each laser-ablated sample underwent analysis of a surface area measuring 300 × 300 μm² for comprehensive assessment. The temperature of the laboratory was 297 ± 1 K, with a relative humidity of 60 % and in normal clean atmospheric conditions.

3. Surface morphology characterization

Morphological analysis of the samples was conducted using Gwyddion 2.59 software [39]. The statistical parameters of 3D surface roughness, according to ISO 25178-2: 2012 standard [22], including height parameters such as root mean square height (S_q), arithmetical mean height (S_a), skewness (S_{sk}), kurtosis (S_{ku}), were thoroughly investigated and analyzed.
The autocorrelation function was expressed as [39]:

$$G(\tau_x,\tau_y)\int\int_{-\infty}^{+\infty} z_1 z_2 w(z_1,z_2,\tau_x,\tau_y)dz_1dz_2 = \lim_{S\to\infty}\frac{1}{S}\int\int_S \xi(x_1,y_1)\xi(x_1+\tau_x,y_1+\tau_y)dx_1dy_1 \quad (1)$$

where z_1 and z_2 are the values of heights at points (x_1, y_1), (x_2, y_2); furthermore, $\tau_x = x_1 - x_2$ and $\tau_y = y_1 - y_2$. The function $w(z_1, z_2, \tau_x, \tau_y)$ denotes the two-dimensional probability density of the random function $\xi(x, y)$ corresponding to points (x_1, y_1), (x_2, y_2), and the distance between these points τ.

The two-dimensional power spectral density function (PSDF) can be written in terms of the Fourier transform of the autocorrelation function as [39]:

$$W(K_x,K_y) = \frac{1}{4\pi}\int\int_{-\infty}^{+\infty} G(\tau_x,\tau_y)e^{-i(K_x\tau_x+K_y\tau_y)}d\tau_x d\tau_y \quad (2)$$

In fractal geometry, the box-counting dimension (D_f), serves as a method for determining the fractal dimension of a set [14]. It is defined by the ratio of the logarithm of the number of boxes of side length ε required to cover the set, denoted as $N(\varepsilon)$, to the logarithm of the reciprocal of the box size ε. Mathematically, it can be expressed as [14]:

$$Df = \lim_{\delta\to 0^+}\frac{\log N(\varepsilon)}{\log(1/\varepsilon)} \quad (3)$$

The fractal dimensions of the surface microtexture of samples were quantified and assessed. A set of the Minkowski Functionals (MFs) that comprises volume (*V(z)*), surface (*S(z)*) and Euler-Poincaré characteristic (or connectivity number *χ(z)*), can be mathematically expressed as [39]:

$$V = N_{white} / N;\ \ S = N_{bound} / N;\ \ \chi = (C_{white} - C_{black}) / N \qquad (4)$$

where: N - the total number of pixels; N_{white} - the number of 'white' pixels, that is pixels above the threshold (pixels below the threshold are referred to as 'black'); N_{bound} - the number of white-black pixel boundaries; C_{white} and C_{black} - the number of continuous sets of white and black pixels respectively. These functions have no units.

4. Results and Discussion

Representative profilometer images of samples under investigation scanned over 300 × 300 μm² surface area and corresponding surface topography are shown in Fig. 1, a-d. After evaluating the profilometer images following adjustments to the laser fluence parameter, noticeable variations in surface topography became apparent, indicating alterations in surface microtexture.

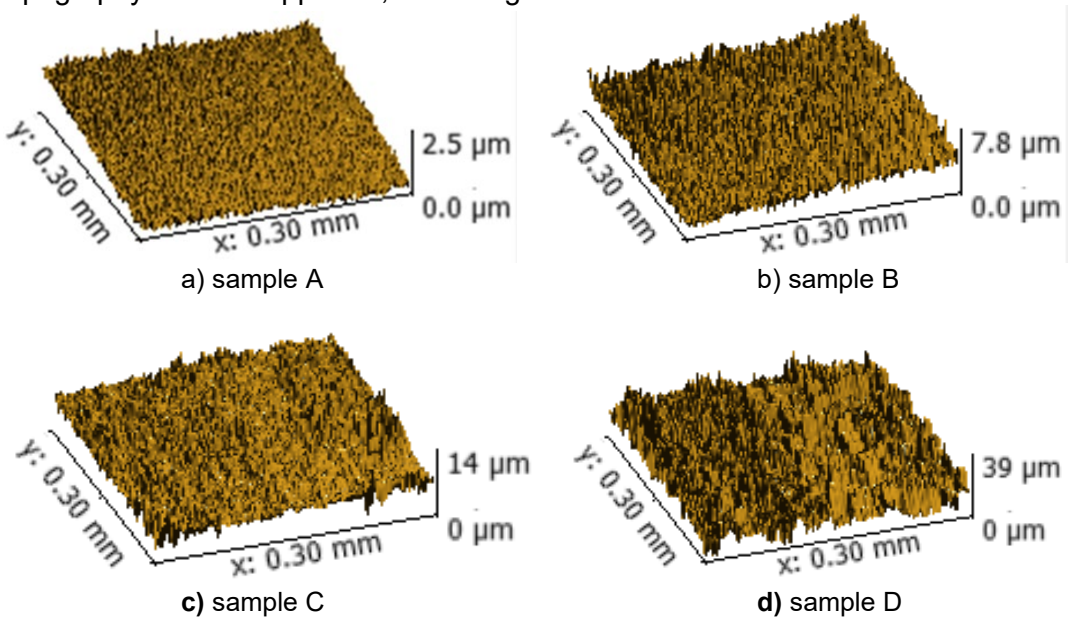

a) sample A b) sample B

c) sample C **d)** sample D

Fig. 1. A set of representative 3-D profilometer images of the Monel® alloy 400 for the scanning areas of 300 × 300 μm²: a) sample A, b) sample B, c) sample C, and d) sample D.

The basic parameters of the height values distribution for surface microtexture offer quantitative measures about the surface topography [14]. In our investigation, these parameters were computed for the analyzed samples according to the guidelines outlined in ISO 25178-2:2012 [22]. A summary of these parameters, including fractal dimensions obtained via the cube counting method [39] using linear interpolation, is shown Table 1. The correlation coefficients (R^2) for all linear fits were 0.992, indicating a good correlation.

Table 2: The basic parameters of the height values distribution of the surface samples

The basic parameters of the height values distribution of the surface samples	Sample A	Sample B	Sample C	Sample D
	Values	Values	Values	Values
(S_a) [μm]	0.351 ± 0.012	0.841 ± 0.017	1.109 ± 0.019	4.170 ± 0.029
(S_q) [μm]	0.414 ± 0.014	1.028 ± 0.021	1.433 ± 0.023	5.250 ± 0.074
Skew (S_{sk}) [-]	0.016 ± 0.003	0.140 ± 0.012	0.317 ± 0.019	0.043 ± 0.005
Kurtosis (S_{ku}) [-]	-0.91 ± 0.06	-0.367 ± 0.04	0.820 ± 0.05	0.088 ± 0.02
Inclination θ [°]	0.3 ± 0.05	1.0 ± 0.15	1.5 ± 0.19	6.8 ± 0.35
Inclination φ [°]	-84.4 ± 0.9	-107.6 ± 1.4	-98.0 ± 1.1	-86.7 ± 0.9
D_f [-]	2.46 ± 0.05	2.48 ± 0.05	2.41 ± 0.05	2.46 ± 0.05

Upon examining Table 2, several remarks can be made: 1) S_a, S_q, S_{sk}, and S_{ku} values generally increase from sample A to sample D, suggesting an increase in surface roughness and complexity; 2) The inclination angles (θ and φ) show variation among the samples, indicating differences in surface orientation; 3) The fractal dimension (D_f) remains relatively consistent across the samples, indicating a similar level of self-similarity in surface structure.

In Fig. 2 are shown the height and slope distribution functions for samples (where p is the corresponding quantity, height or slope; and abscissa is the tangent of the angle), computed as non-cumulative (i.e. densities). By analyzing these aspects across samples A, B, C, and D, differences in the graphs of the height distribution functions can be discerned, providing insights into their respective surface characteristics. The parameter p exhibits a decrease in the peak value from sample A (p_{max} = 0.81 μm^{-1}) to sample D (p_{max} = 0.08 μm^{-1}). Additionally, it's evident that the graphs depicting the slope distribution functions for the samples exhibit symmetry (in report of the value of tan β = 0), while the parameter p exhibits a decrease in the peak value from sample A (p_{max} = 6.4) to sample D (p_{max} = 0.58).

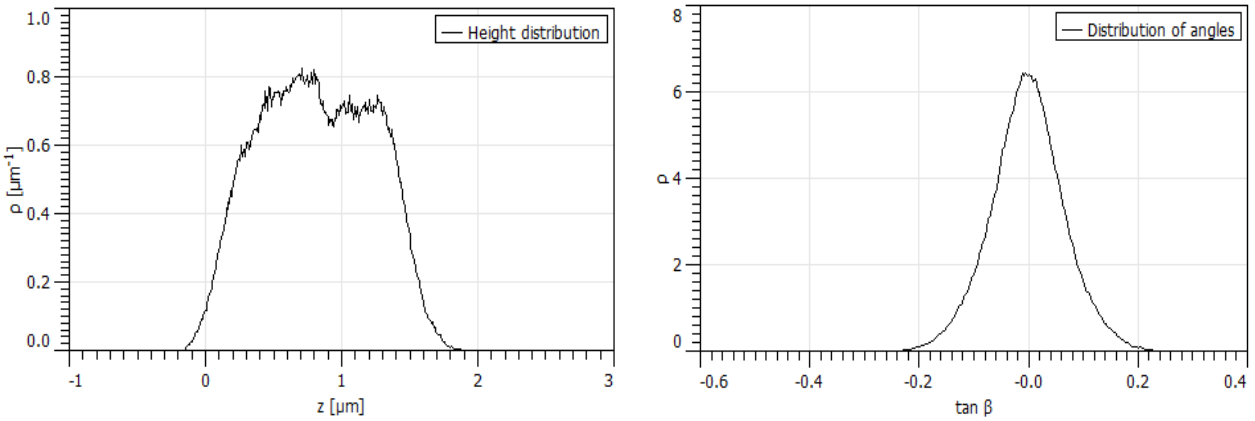

a) Sample A

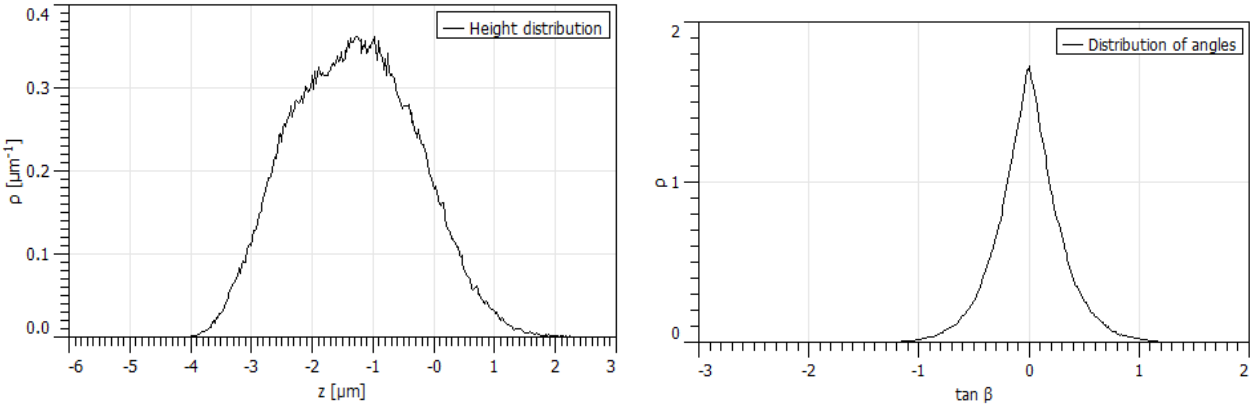

b) Sample B

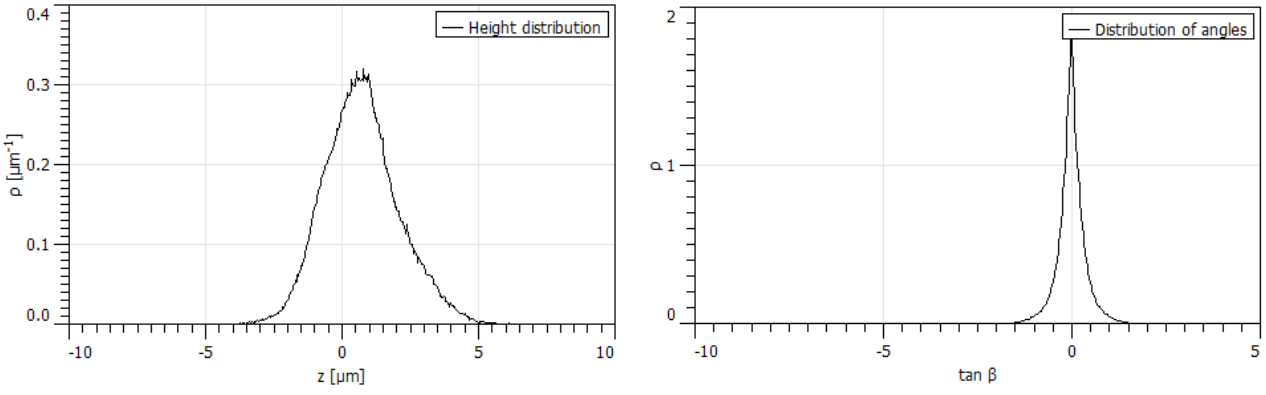

c) Sample C

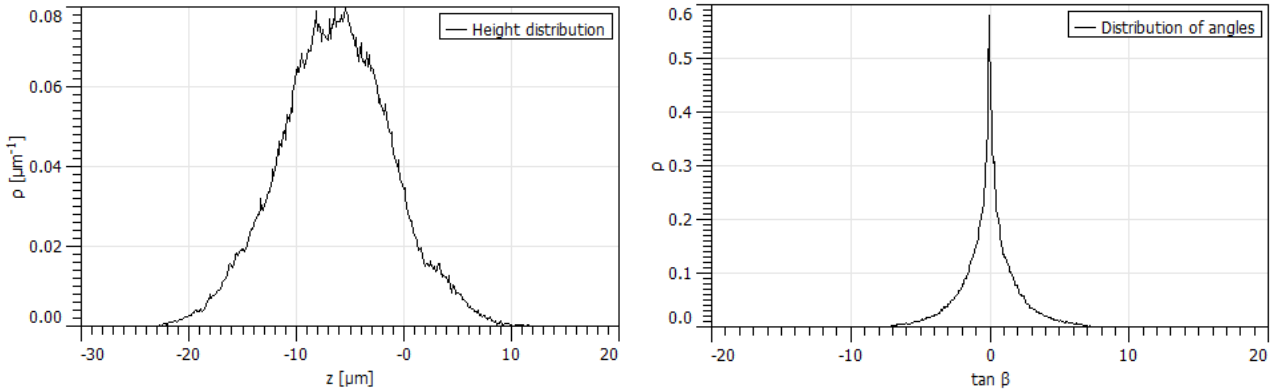

d) Sample D

Fig. 2. The height and slope distribution functions computed as non-cumulative, in horizontal direction. (where *p* is the corresponding quantity, height or slope; and abscissa is the tangent of the angle), for: a) sample A, b) sample B, c) sample C, and d) sample D. Scanning areas of 300 × 300 µm².

Figure 3 depicts graphs of the autocorrelation function (ACF or G), and the height-height correlation function (HHCF or H), based on the linear interpolation type, for the samples, shown in horizontal direction. In the context of surface analysis, the ACF quantifies how much a surface profile at one point correlates with itself at another point as the distance between them varies. In the context of surface analysis, linear interpolation is often used to create a smoother representation of the surface profile or correlation functions. It is evident that the highest value of the parameter G_{max} for all samples is found for 0.0 mm ≤ τ ≤ 0.01 mm. The height-height correlation function specifically focuses on the correlation between height values at different points on the surface. Like the ACF, the H function helps characterize surface roughness and surface features (such as roughness, periodicity, and texture). It can be seen that the highest value of the parameter H_{max} for all samples is found for 0.2 mm ≤ τ ≤ 0.3 mm, while the lowest value of the parameter H_{min} for all samples is found for 0.0 mm ≤ τ ≤ 0.01 mm.

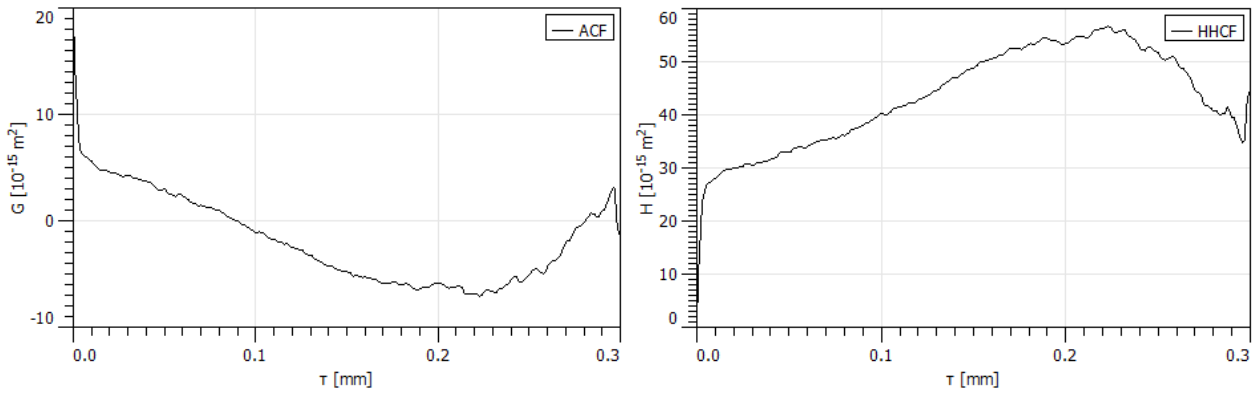

a) Sample A

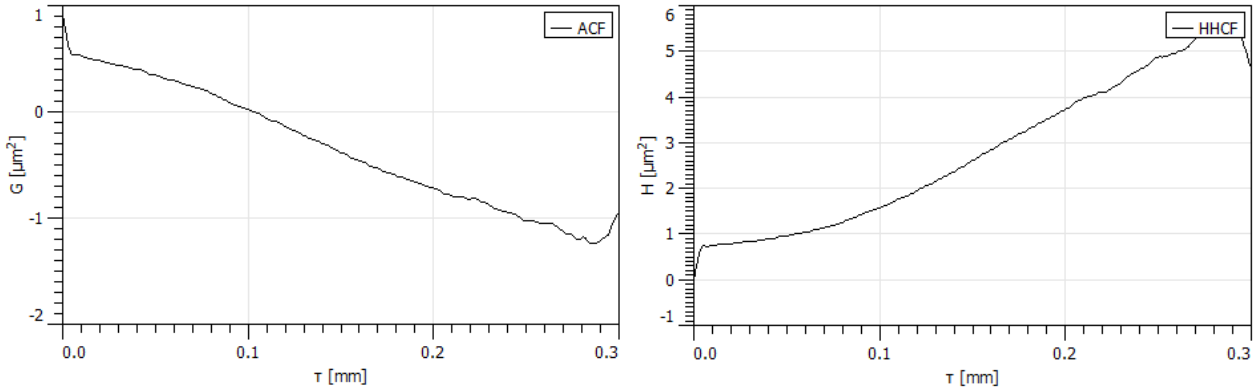

b) Sample B

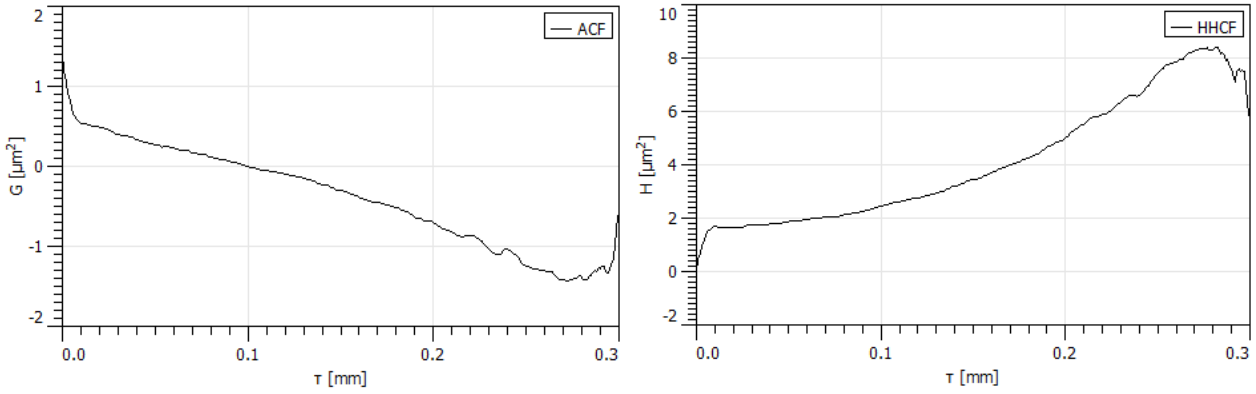

c) Sample C

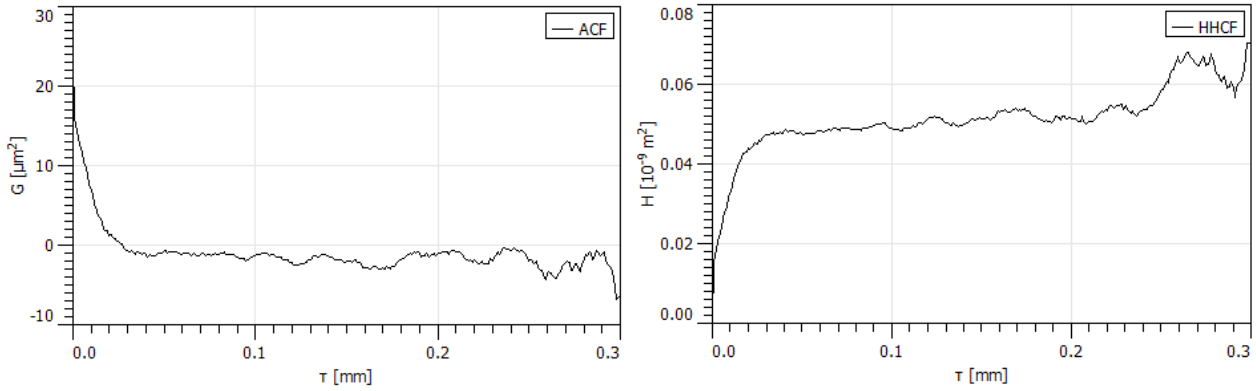

d) Sample D

Fig. 3. The autocorrelation function (G), the height-height correlation function (H), based on the linear interpolation type, for: a) sample A, b) sample B, c) sample C, and d) sample D. Scanning areas of 300 × 300 µm².

In Figure 4, the two-dimensional power spectral density function (PSDF) of the samples is illustrated. It is clear that the highest value of the parameter W_1 for all samples is found for 0.0 µm^{-1} ≤ k ≤ 0.01 µm^{-1}.

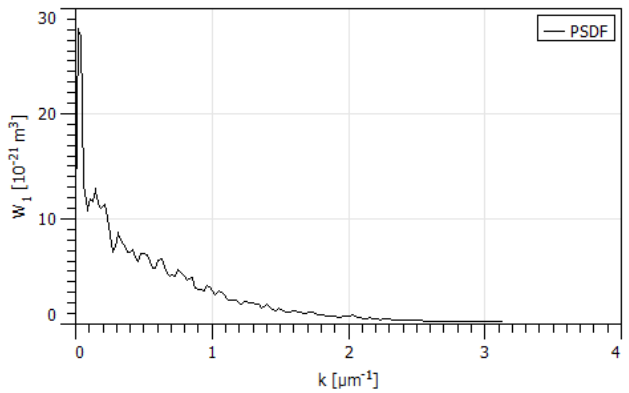

a) Sample A

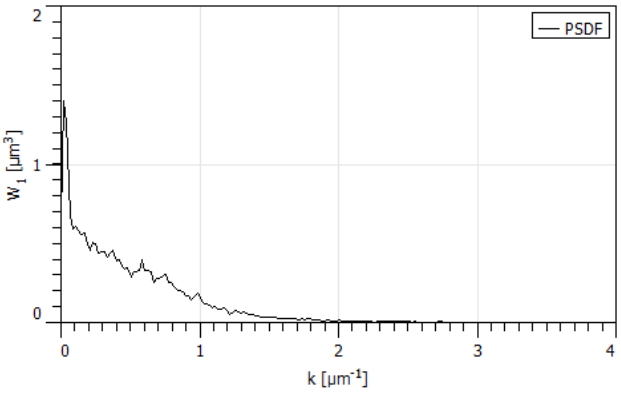

b) Sample B

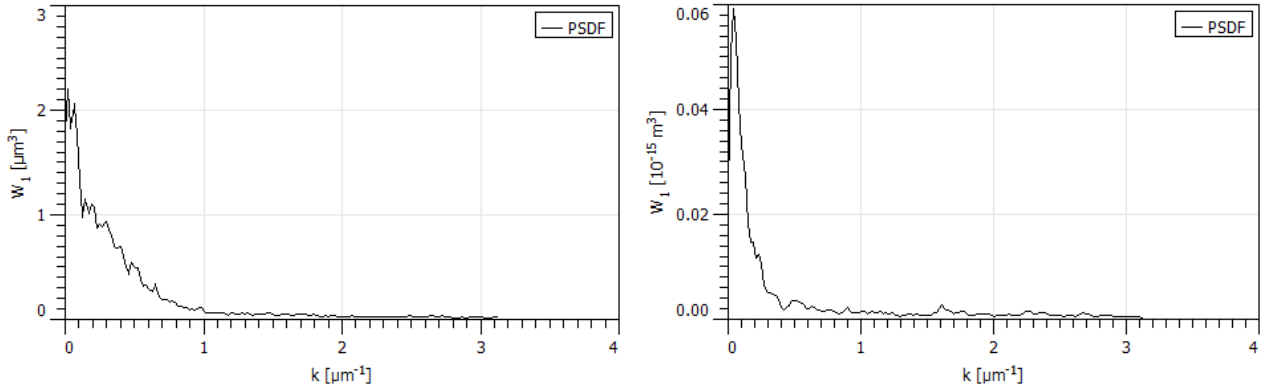

c) Sample C d) Sample D

Fig. 4. The two-dimensional power spectral density function (PSDF) for: a) sample A, b) sample B, c) sample C, and d) sample D. Scanning areas of 300 × 300 µm².

Figs. 5, 6 & 7 show the plots of MFs functions *V(z)*, *S(z)*, and *χ(z)* (these functions are unitless).

In Figure 5, the Minkowski volume *V(z)* of the samples is illustrated. Notably, the range of *V(z)* falls within 0 ≤ *V(z)* ≤ 1 across all samples. Sample A demonstrates the narrowest range for *z* [µm] (-0.2 µm ≤ *z* ≤ 1.6 µm), while sample D exhibits the widest range for *z* [µm] (-24 µm ≤ *z* ≤ 16 µm).

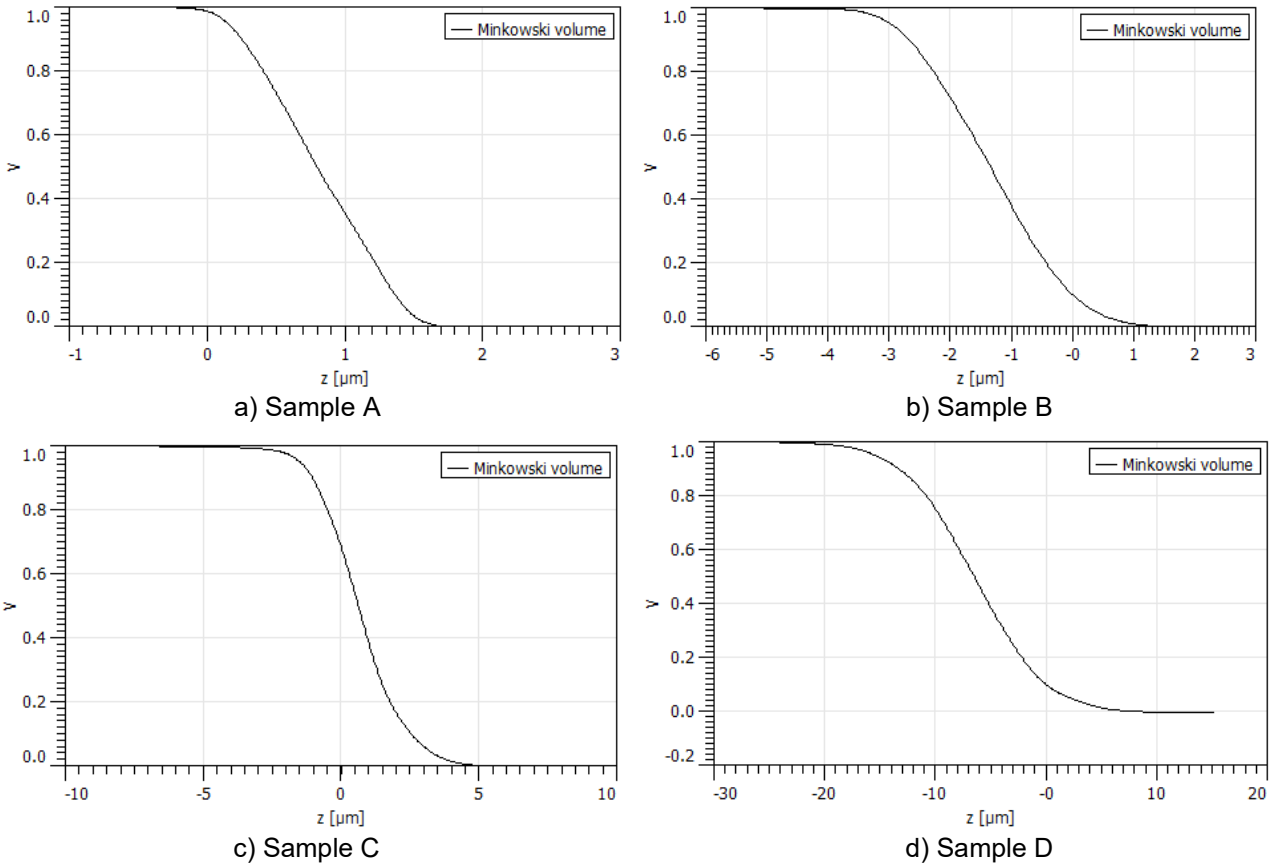

a) Sample A b) Sample B

c) Sample C d) Sample D

Fig. 5. The Minkowski volume *V(z)*, for: a) sample A, b) sample B, c) sample C, and d) sample D. Scanning areas of 300 × 300 µm². These functions have no units.

In Figure 6, the Minkowski surface *S(z)* of the samples is depicted. Notably, the highest value of the peak parameter S_{max} = 0.22 [-] is observed in sample D, while the lowest value of the peak parameter S_{min} = 0.062 [-] is observed in sample A. Sample A demonstrates the narrowest range for *z* [µm] (-0.2 µm ≤ *z* ≤ 1.9 µm), whereas sample D exhibits the widest range for *z* [µm] (-22 µm ≤ *z* ≤ 10 µm).

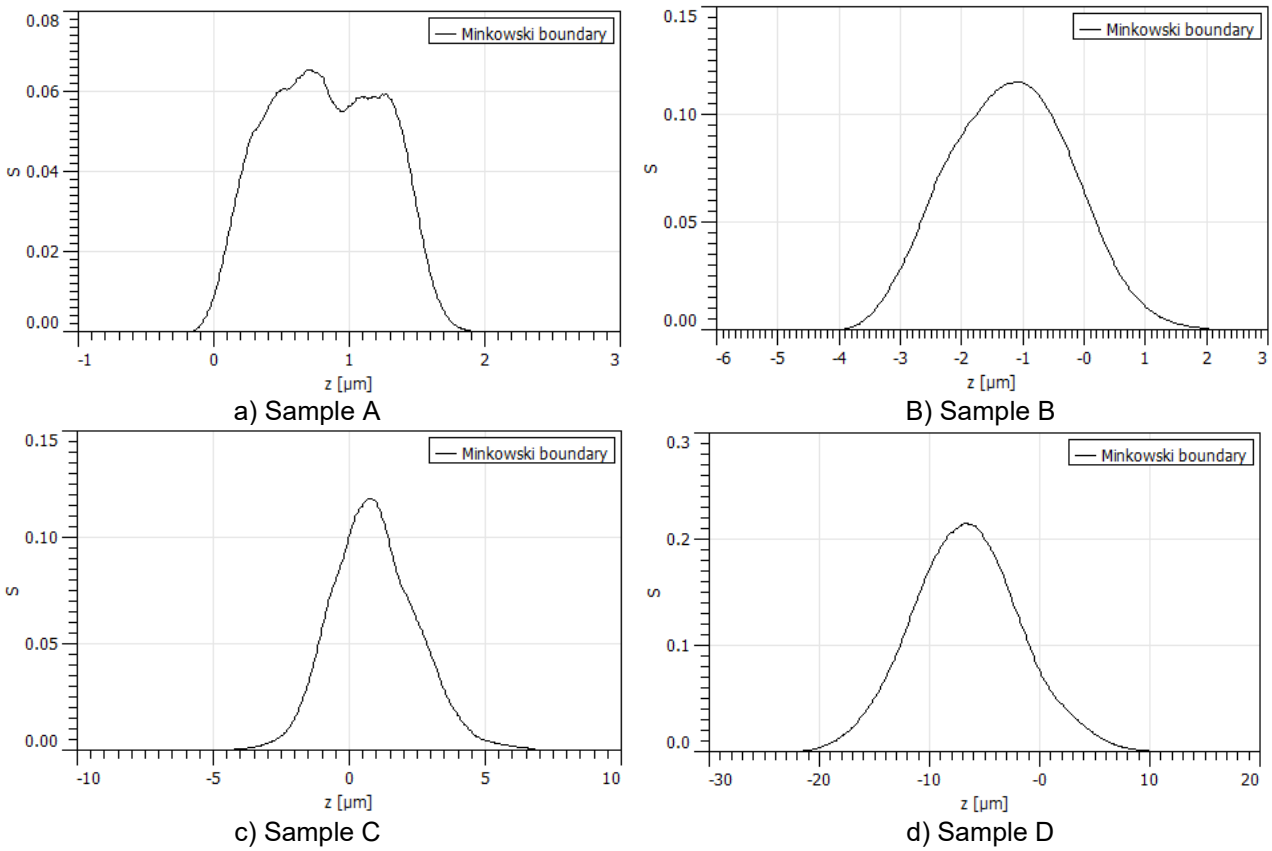

a) Sample A B) Sample B

c) Sample C d) Sample D

Fig. 6. The Minkowski surface *S(z)*, for: a) sample A, b) sample B, c) sample C, and d) sample D. Scanning areas of 300 × 300 µm².

In Figure 7, the Minkowski connectivity, number $\chi(z)$, of the samples is depicted. Notably, the highest value of the peak parameter χ_{max} = 0.42 [-] is observed in sample A, while the lowest value of the peak parameter χ_{min} = -0.38 [-] is observed in sample D. Sample A demonstrates the narrowest range for z [µm] (-0.3 µm ≤ z ≤ 2.2 µm), whereas sample D exhibits the widest range for z [µm] (-26 µm ≤ z ≤ 16 µm).

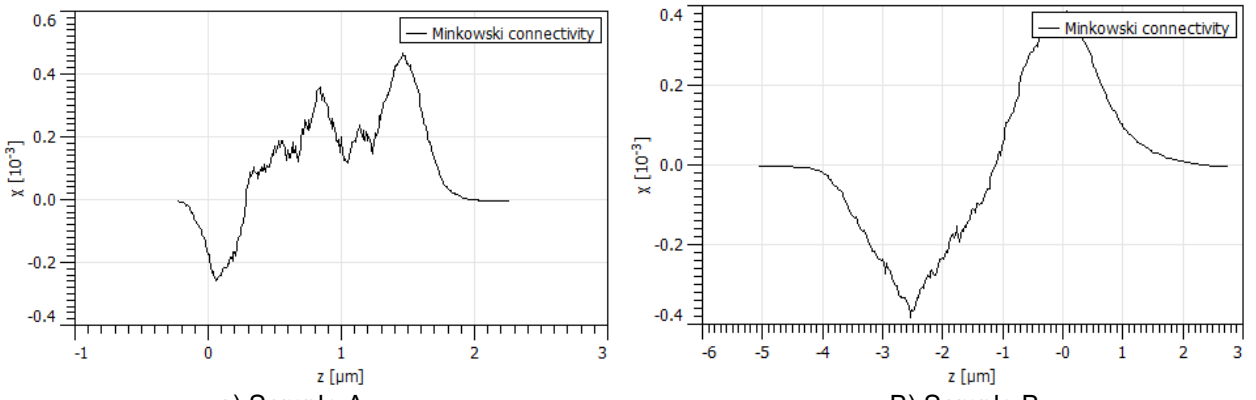

a) Sample A B) Sample B

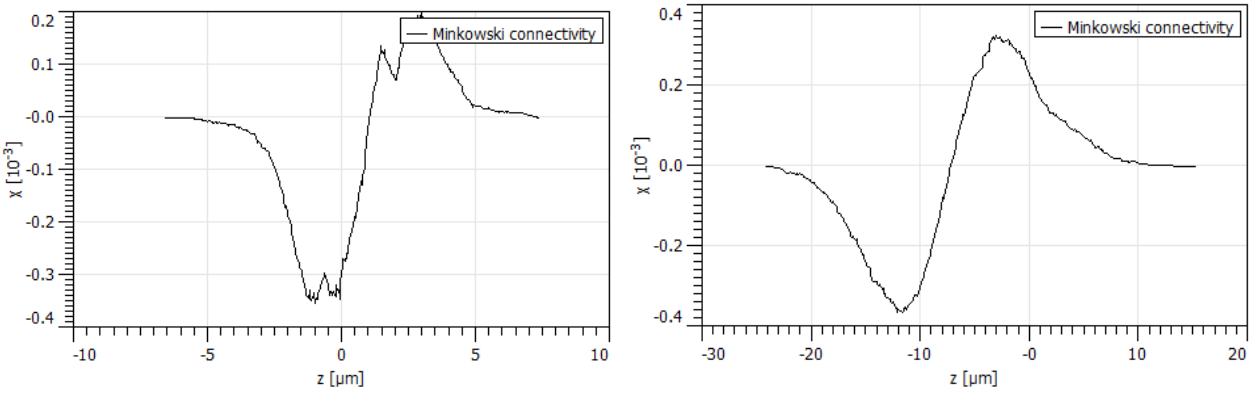

c) Sample C d) Sample D

Fig. 7. The Minkowski connectivity, number *χ(z)*, for: a) sample A, b) sample B, c) sample C, and d) sample D. Scanning areas of 300 × 300 µm².

Conclusions

This study investigated the impact of picosecond laser ablation on the surface morphology of Monel® alloy 400, a nickel-copper alloy widely used in marine equipment components. Through a series of experiments involving mechanical preparation, laser processing, and surface analysis, the study explored the intricate relationship between laser parameters and surface characteristics. Profilometry analysis revealed significant variations in surface topography among samples, indicating distinct microtexture alterations post-laser treatment. Height and slope distribution functions were analyzed, uncovering differences in surface features and peak values across samples. The MFs provided quantitative measures of geometric properties, offering insights into sample-specific variations in surface morphology. The findings contribute to optimizing laser processing techniques for Monel® alloy 400 enhancing the performance of marine equipment components.

Conflicts of Interest: The author declares no conflict of interest.

ORCIDs:
Ştefan Ţălu, https://orcid.org/0000-0003-1311-7657.
Kipkurui Ronoh, https://orcid.org/0000-0002-6867-1201
Dinara Sobola, https://orcid.org/0000-0002-0008-5265

Author Contributions: Ştefan Ţălu: methodology, data curation, data analysis, resources, software, supervision, writing–original draft, writing-review and editing. Kipkurui Ronoh: conceptualization, methodology, data curation, writing–original draft, and formal analysis. Dinara Sobola: conceptualization, project administration, validation. All authors have read and agreed to the published version of the manuscript.

Acknowledgements: We acknowledge CzechNanoLab Research Infrastructure supported by MEYS CR (LM2023051). The research was supported by the Czech Academy of Sciences (RVO: 68081731).

References

[1] Monel® Alloy 400. Accessed April 10, 2024. https://megamex.com/monel-400/.
[2] Zhu, Yuhua, Jianzhang Wang, Hao Liu, Pengwei Ren, and Fengyuan Yan. "The tribocorrosion behavior of Monel 400 alloy in seawater at different temperatures." *Tribology International* 189 (November 2023): 108975.
[3] Zhu, Yuhua, Jianzhang Wang, Hao Liu, Pengwei Ren, and Fengyuan Yan. "Effect of dissolved oxygen content on tribo-corrosion behavior of Monel 400 alloy in seawater." *Metals* 14, no. 1 (2024): 6.
[4] Ronoh, Kipkurui, Jan Novotný, Libor Mrňa, Alexandr Knápek, and Dinara Sobola. "Effects of laser and scanning parameters on surface modification of MONEL® alloy 400 by picosecond laser." *Optics & Laser Technology* 172 (May 2024): 110514.
[5] Rajčić, Boris, Sanja Petronić, Katarina Čolić, Zoran Stević, Ana Petrović, Žarko Mišković, and Dubravka Milovanović. "Laser processing of Ni-based superalloy surfaces susceptible to stress concentration." *Metals* 11, no. 5 (2021): 750.
[6] Raffeis, Iris, Frank Adjei-Kyeremeh, Uwe Vroomen, Elmar Westhoff, Sebastian Bremen, Alexandru Hohoi, and Andreas Bührig-Polaczek. "Qualification of a Ni–Cu alloy for the laser powder bed fusion process (LPBF): its microstructure and mechanical properties." *Applied Sciences* 10, no. 10 (2020): 3401.

[7] Ahmad, Zaki. 'Selection of materials for corrosive environment.' In *Principles of corrosion engineering and corrosion control*, 1st edition. Butterworth-Heinemann, 2006, pp. 479–549.
[8] Kukliński, Mateusz, Aneta Bartkowska, and Damian Przestacki. "Microstructure and selected properties of Monel 400 alloy after laser heat treatment and laser boriding using diode laser." *International Journal of Advanced Manufacturing Technology* 98 (2018): 3005-3017.
[9] Kukliński, Mateusz, Aneta Bartkowska, Damian Przestacki, and Grzegorz Kinal. "Influence of microstructure and chemical composition on microhardness and wear properties of laser borided Monel 400." *Materials* 13, no. 24 (2020): 5757.
[10] Oșan, Andrei. "Experimental research on the processing of concave spherical surfaces with toroidal mills versus spherical mills." *Hidraulica Magazine*, no. 1 (March 2020): 7-15.
[11] Lazăr, Iosif, Ilare Bordeasu, Mircea O. Popoviciu, and Lavinia Madalina Micu. "Researches regarding the behavior of CuAl10.5Ni5Fe4.8Mn1.5 at erosion generated by vibratory cavitation." *Hidraulica Magazine*, no. 4 (December 2017): 25-33.
[12] Ravai-Nagy, Sandor, and Nicolae Medan. "Liquid study of surface roughness for steel parts cut with abrasive water jets." *Hidraulica Magazine*, no. 4 (December 2016): 12-17.
[13] Rostami, Amir, and Jeffrey L. Streator. "Liquid film adhesion in contact between rough surfaces." *Hidraulica Magazine*, no. 3 (September 2015): 27-31.
[14] Ţălu, Ştefan. *Micro and nanoscale characterization of three dimensional surfaces. Basics and applications*. Cluj-Napoca, Napoca Star Publishing House, 2015.
[15] Basarman, Adrian Paul, and Nicolae Medan. "Comparative study of the AWJ cutting geometry using the 3D point measuring method versus 3D scanning of the surfaces." *Hidraulica Magazine*, no. 2 (June 2017): 34-39.
[16] Bordeasu, Ilare, Mircea Octavian Popoviciu, Ion Mitelea, Lavinia Madalina Micu, Octavian Victor Oanca, C-tin Bordeasu, Laura Cornelia Salcianu, and Cristian Ghera. "Cavitation erosion resistance of AMPCO 45 Bronze with heat treatments." *Hidraulica Magazine*, no. 2 (June 2014): 53-61.
[17] Ţălu, Ştefan, Ram Pratap Yadav, Ashok Kumar Mittal, Ali Arman, Carlos Luna, Amine Achour, Mohsen Mardani, Azin Ahmadpourian, Sirvan Naderi, Ali Asghar Zavarian, Fatemeh Hafezi, Ali Saghi, Alia Méndez, and Gabriel Trejo. "Application of Mie theory and fractal models to determine the optical and surface roughness of Ag-Cu thin films." *Optical and Quantum Electronics* 49, no. 256 (2017): 1-15.
[18] Ţălu, Ştefan, Miroslaw Bramowicz, Slawomir Kulesza, Atefeh Ghaderi, Shahram Solaymani, Hadi Savaloni, and Reza Babaee. "Micromorphology analysis of specific 3-D surface texture of silver chiral nanoflower sculptured structures." *Journal of Industrial and Engineering Chemistry* 43 (November 2016): 164-169.
[19] Ţălu, Ştefan, Robert Saraiva Matos, Erveton Pinheiro Pinto, Sahar Rezaee, and Mohsen Mardani. "Stereometric and fractal analysis of sputtered Ag-Cu thin films." *Surfaces and Interfaces* 21 (December 2020): 100650.
[20] Solaymani, Shahram, Slawomir Kulesza, Ştefan Ţălu, Miroslaw Bramowicz, Negin Beryani Nezafat, Vali Dalouji, Sahar Rezaee, Hossein Karami, Mohammad Malekzadeh, and Elham Soltanpanah Dorbidi. "The effect of different laser irradiation on rugometric and microtopographic features in zirconia ceramics: study of surface statistical metrics." *Journal of Alloys and Compounds* 765 (October 2018): 180-185.
[21] Dejam, Laya, Slawomir Kulesza, Jamshid Sabbaghzadeh, Atefeh Ghaderi, Shahram Solaymani, Ștefan Țălu, Miroslaw Bramowicz, Mitra Amouamouha, Amir Hossein Salehi Shayegan, and Amir Hossein Sari. "ZnO, Cu-doped ZnO, Al-doped ZnO and Cu-Al doped ZnO thin films: Advanced micro-morphology, crystalline structures and optical properties." *Results in Physics* 44 (January 2023): 106209.
[22] ISO 25178-2:2012. Geometrical Product Specifications (GPS) - Surface Texture: Areal - Part 2: Terms, Definitions and Surface Texture Parameters. Accessed April 18, 2024. http://www.iso.org.
[23] Ţălu, Ştefan, Papež Nikola, Dinara Sobola, Amine Achour, and Shahram Solaymani. "Micromorphology investigation of GaAs solar cells: Case study on statistical surface roughness parameters." *Journal of Materials Science: Materials in Electronics* 28, no. 20 (2017): 15370–15379.
[24] Dejam, Laya, Shahram Solaymani, Amine Achour, Sebastian Stach, Ştefan Ţălu, Negin Beryani Nezafat, Vali Dalouji, Ali Asghar Shokri, and Atefeh Ghaderi. "Correlation between surface topography, optical band gaps and crystalline properties of engineered AZO and CAZO thin films." *Chemical Physics Letters* 719 (March 2019): 78-90.
[25] Das, Abhijeet, Vipin Chawla, Robert Saraiva Matos, Henrique Duarte Da Fonseca Filho, Ram Pratap Yadav, Ştefan Ţălu, and Sanjeev Kumar. "Surface microtexture and wettability analysis of quasi two-dimensional (Ti, Al)N thin films using fractal geometry." *Surface and Coatings Technology* 421 (September 2021): 127420.
[26] Ţălu, Ştefan, Niranjan Patra, and Marco Salerno. "Micromorphological characterization of polymer-oxide nanocomposite thin films by atomic force microscopy and fractal geometry analysis." *Progress in Organic Coatings* 89 (December 2015): 50-56.

[27] Ţălu, Ştefan, Sebastian Stach, Joana Zaharieva, Maria Milanova, Dimitar Todorovsky, and Stefano Giovanzana. "Surface roughness characterization of poly(methylmethacrylate) films with immobilized Eu(III) β-Diketonates by fractal analysis." *International Journal of Polymer Analysis and Characterization* 19, no. 5 (2014): 404-421.

[28] Ţălu, Ştefan, Sebastian Stach, Shahoo Valedbagi, Reza Bavadi, S. Mohammad Elahi, and Mihai Ţălu. "Multifractal characteristics of titanium nitride thin films." *Materials Science-Poland* 33, no. 3 (2015): 541-548.

[29] Ţălu, Ştefan, and Sebastian Stach. "Multifractal characterization of unworn hydrogel contact lens surfaces." *Polymer Engineering and Science* 54, no. 5 (May 2014): 1066-1080.

[30] Shakoury, Reza, Ali Arman, Fredrick Mwema, Carlos Luna, Koushik Ghosh, Stanislav Jurečka, Ştefan Ţălu, Sahar Rezaee, and Alireza Grayeli Korpi. "Multifractal and optical bandgap characterization of Ta2O5 thin films deposited by electron gun method." *Optical and Quantum Electronics* 52, no. 2, (2020): 95.

[31] Ţălu, Ştefan, Sebastian Stach, Tijana Lainović, Marko Vilotić, Larisa lažić, Sandu Florin Alb, and Damir Kakaš. "Surface roughness and morphology of dental anocomposites polished by four different procedures evaluated by a multifractal approach." *Applied Surface Science* 330 (March 2015): 20-29.

[32] Grayeli Korpi, Alireza, Ştefan Ţălu, Miroslaw Bramowicz, Ali Arman, Slawomir Kulesza, Bartosz Pszczolkowski, Stanislav Jurečka, Mohsen Mardani, Carlos Luna, Parvin Balashabadi, Sahar Rezaee, and Sabavath Gopikishan. "Minkowski functional characterization and fractal analysis of surfaces of titanium nitride films." *Materials Research Express* 6, no. 8 (2019): 086463.

[33] Ţălu, Ştefan. "Characterization of surface roughness of unworn hydrogel contact lenses at a nanometric scale using methods of modern metrology." *Polymer Engineering and Science* 53, no. 10 (October 2013): 2141-2150.

[34] Matos, Robert S., Nilson S. Ferreira, Ştefan Ţălu, Atefeh Ghaderi, Shahram Solaymani, Marcelo A. Pires, Edgar Aparecido Sanches, and Henrique D. da Fonseca Filho. "Percolative, multifractal, and symmetry properties of the surface at nanoscale of Cu-Ni bimetallic thin films deposited by RF-PECVD." *Symmetry* 14, no. 12 (2022): 2675.

[35] Pinheiro Pinto, Erveton, Robert S. Matos, Marcelo A. Pires, Lucas Dos Santos Lima, Ştefan Ţălu, Henrique Duarte Da Fonseca Filho, Shikhgasan Ramazanov, Shahram Solaymani, and Claudio Larosa. "Nanoscale 3D spatial analysis of zirconia disc surfaces subjected to different laser treatments." *Fractal Fract*. 7, no. 2 (2023): 160.

[36] Sadeghi, Mohammad, Amir Zelati, Sahar Rezaee, Carlos Luna, Robert Saraiva Matos, Marcelo Amanajás Pires, Nilson S. Ferreira, Henrique Duarte da Fonseca Filho, Azin Ahmadpourian, and Ştefan Ţălu. "Evaluating the Topological Surface Properties of Cu/Cr Thin Films Using 3D Atomic Force Microscopy Topographical Maps." *Coatings* 12, no. 9 (2022): 1364.

[37] Ronoh, Kipkurui, Dinara Sobola, Libor Mrňa, Jan Novotný, Rashid Dallaev, Alexandr Knápek, Vladimír Kolařík, and Vladimír Holcman. "Characterization of the picosecond laser-ablated HOPG using Raman spectroscopy and SEM microscopy." *Materials Today Communications* 14 (March 2023): 105181.

[38] Ronoh, Kipkurui, Jan Novotný, Libor Mrňa, Alexandr Knápek, and Dinara Sobola. "Surface Structuring of the CP Titanium by Ultrafast Laser Pulses." *Applied Sciences* 14, no. 8 (2024): 3164.

[39] Gwyddion software. (Accessed April 10, 2024). Available online: http://gwyddion.net